Hindawi
International Journal of Electrochemistry
Volume 2018, Article ID 9875438, 12 pages
https://doi.org/10.1155/2018/9875438

Research Article

Spiky Nickel Electrodes for Electrochemical Oxygen Evolution Catalysis by Femtosecond Laser Structuring

Felix Rieck genannt Best,[1] Jürgen Koch,[2] Gerhard Lilienkamp,[3] Franz Körkemeyer,[4] Hans Jürgen Maier,[4] Jürgen Caro,[1] and Karsten Lange[1]

[1]*Institute of Physical Chemistry and Electrochemistry, Leibniz Universität Hannover, Callinstr. 3A, 30167 Hannover, Germany*
[2]*Laser Zentrum Hannover e.V., Hollerithallee 8, 30419 Hannover, Germany*
[3]*Institute of Energy Research and Physical Technologies, TU Clausthal, Leibnizstr. 4, 38678 Clausthal-Zellerfeld, Germany*
[4]*Institut für Werkstoffkunde (Material Science), Leibniz Universität Hannover, An der Universität 2, 30823 Garbsen, Germany*

Correspondence should be addressed to Karsten Lange; karsten.lange@pci.uni-hannover.de

Received 17 August 2018; Accepted 22 October 2018; Published 19 November 2018

Guest Editor: Jinmei Liu

Micro- and nanostructured Ni/NiO surfaces were generated by femtosecond laser structuring for oxygen evolution reaction in alkaline water electrolysis cells. For two different angles between the laser beam and the nickel surface, two different types of laser-structured electrodes were prepared, characterized, and compared with a plane tempered nickel electrode. Their electrochemical activities for the oxygen evolution reaction were tested by using cyclic and linear sweep voltammetry. The chemical surface composition was investigated by X-ray photoelectron spectroscopy. Laser structuring increased the overall electrochemical performance by more than one order of magnitude. The overpotential of the laser-structured electrodes for the oxygen evolution reaction was decreased by more than 100 mV due to high defect densities of the structures created by the laser ablation process.

1. Introduction

Water electrolysis provides a simple and clean method to produce hydrogen using renewable energies, while both water and the energy source (wind and solar energy) are practically infinite. In alkaline water electrolysis, two important reactions take place: the hydrogen evolution reaction (HER) at the cathode and simultaneously the oxygen evolution reaction (OER) at the anode. Platinum shows the best catalytic activity for the HER [1, 2]. Due to its high price, platinum is in most cases replaced in industrial alkaline water electrolysis cells by cathodes made of stainless steel or high-area nickel on steel [3]. However, the efficiency of the water electrolysis cell is limited by the sluggish anodic kinetics of the OER compared to the HER [4, 5]. IrO_2 and RuO_2 are considered to be state-of-the-art electrode material for the OER, as they show the lowest overpotentials [6, 7]. Consequently, the high cost and the lack of long-term stability in alkaline water electrolysis conditions prevent an industrial application and lead to the search for different cost-efficient and highly active catalysts for the OER [8]. First-row transition metal oxides, like nickel [9], cobalt [10], iron [11], and manganese [12] oxides and mixed oxides in the spinel [13] and perovskite [14] structure seem to fit the demands for OER anode active materials.

The overall efficiency of a water electrolysis cell is determined by the combined resistances of all components and chemical processes. In addition to the electrode materials and the resulting overpotential, mass transport problems always occur during reactions in aqueous solution [15]. Apart from mass transfer, temperature distribution, bubble size, and bubble detachment affect the potential and current density distribution in a gas evolution cell [16, 17]. Thus, the bubble attachment will affect the efficiency adversely by blocking the catalytic active sites of the electrode [18]. Calculations show that the energy loss caused by bubbles is the major contributor to the total energy loss of a gas evolution cell [16]. Forced electrolyte convection, supergravity [19], and ultrasonication [20] are ways to address the problem of bubble attachment, although the electrolyte management cost would increase

and additional energy consumption would arise. Therefore, researchers are focusing on electrode design to facilitate gas bubble detachment from the electrode [21–23]. A superhydrophilic electrode surface would attract the electrolyte more than the bubbles and decrease the bubble-electrode surface attraction, accordingly smaller bubbles would detach easier on their own [24, 25]. Another approach to reduce the forces, that hold the bubble at the surface, is to minimize the bubble-electrode contact area. There are several studies, which utilize the nanostructuring of gas evolution electrodes to create "superaerophobic" surfaces [17, 26–28]. However, creating electrodes with nanowire surfaces is difficult to implement in an industrial-scale fabrication process for gas evolution electrodes.

Modern femtosecond lasers represent a new powerful tool for customized electrode structuring. Specifically, the generation of ordered nano- and microstructures on bulk substrates is an upscalable process for large-area applications, thanks to recently available high power femtosecond lasers [30, 31]. Via the high variety of process parameters, the surface morphology can be customized. One type of laser-induced self-organized surface structures is the micrometer-sized cone-like protrusions (CLPs, also often called spike structures), which are superimposed by nanostructures [32–37].

CLPs are stochastically ordered structures oriented antiparallel to the direction of the incident laser beam. Their heights, flank angles, and average distances can be controlled by choosing process parameters such as laser fluence, laser wavelength, and environmental conditions. Furthermore, they are influenced by material properties. CLPs can be processed on many metals [38–40] and semiconductors [41, 42]. Suitable lasers are pulsed lasers with nanosecond (ns) down to femtosecond (fs) pulse duration. In general, shorter pulse durations prevent melting and lead to higher surface area [43, 44]. The process of CLP formation is not yet fully understood. The formation of CLPs is done with a laser focus diameter of around 10 μm or bigger and a relatively high laser fluence of usually a few 10 J cm^{-2}. Since the CLPs are directed antiparallel to the incident laser beam, tilting the workpiece surface leads to CLPs with the same tilting angle [45, 46] but requires higher laser pulse energy.

The main objective of the present study was to enlarge the surface area and simultaneously activate the Ni electrode for high current density OER application via our femtosecond laser structuring approach. Blank Ni plates were used as substrate material, which were polished and afterwards structured by femtosecond laser pulses under irradiation angles of 0° or 45° to create two different types of Ni CLPs electrodes. The topography of the sample surfaces was studied with the help of scanning electron microscopy and X-ray microscopy. In addition, the chemical compositions of the surfaces were investigated by X-ray photoelectron spectroscopy. The electrodes were placed vertically in a reactor cell and were characterized by cyclic and linear sweep voltammetry to determine the accessible surface area and the activity for the OER with realistic gas bubble behavior.

2. Experimental Section

2.1. Electrode Preparation. First the Ni plates (Alfa Aesar) with a size of 10 mm × 10 mm were polished with a Phoenix 4000 polishing machine using 15 μm, 6 μm, 3 μm, and 1 μm diamond suspensions (Buehler) and cleaned with acetone and ultra-pure water. Afterwards the plates were either tempered or laser structured. The reference sample had been tempered at 650°C in air for 1 h with a heating rate of 5°C min^{-1}. The irradiation angle of the laser was set to 0° or 45°, to create two different types of CLP structures.

The laser structuring was performed with a femtosecond laser system (Femtopower Compact Pro, Femtolasers Produktions GmbH) with a fundamental wavelength of 800 nm, a sub-30 fs pulse duration, and a pulse repetition rate of 1 kHz. The laser pulses were focused using an achromatic lens with 200 mm focal distance resulting in a focus with Gaussian intensity distribution and a $1/e^2$ diameter of 34 μm. The compressor of the laser system was adjusted for shortest pulse duration in the focus. The linear polarization was constantly rotated at 800 rpm using a motorized rotation mount with a half wave plate placed in the beam path in front of the focusing optics. A XYZ-positioning system (Physik Instrumente) controlled by laser machining software and synchronized with laser switching was used for sample movement and focus positioning. The focus position was set onto the sample surface. In case of the 45° incident laser beam, the sample was placed on a 45° holder mounted to the XY-stage with the Z-stage keeping the focus constantly on the sample surface. It was possible to almost completely prevent accumulation of ablation particles on the sample surface by a combination of a compressed air cross jet, particle fume extraction, and by choosing process parameters optimized for particle generation with high kinetic energy. Processing was done in the form of hatch patterns consisting of parallel lines with constant line-to-line distance. Processing directions were alternated from line to line. After the completion of every hatch pattern the orientation was rotated by 90° before the next hatch pattern was scanned. This process was repeated eight times. Different processing parameters were tested for achieving dense and uniformly distributed CLP topographies. Table 1 lists the processing parameters for the Ni CLPs 0° and the Ni CLPs 45° sample.

2.2. Physical Characterization. The topography of the laser-structured surfaces was studied by scanning electron microscopy (SEM) on a JEOL JSM-6700F operating at 2 kV and 10 μA. The SEM was coupled with an energy-dispersive X-ray (EDX) detector. X-ray diffraction (XRD) patterns were acquired on a Bruker D8 Advance diffractometer operating at 40 kV and 40 mA with Cu-K_α-radiation (λ = 0.154 nm). The X-ray photoelectron spectroscopy (XPS) was performed with nonmonochromatized Al-K_α-radiation. A hemispherical analyzer (Omnicron GmbH) with 20 eV pass energy and an acquisition time of 10 s per energy step of 100 meV was used. The X-ray microscopy (XRM) was performed using a Zeiss Xradia Versa 520. The X-rays were generated by a Nordson DAGE NT100 transmissive source with a tungsten target

Table 1: Processing parameters for the laser-structured samples Ni CLPs 0° and Ni CLPs 45°.

Sample name	Laser pulse energy	Laser peak fluence	Sample movement velocity	Hatch line-to-line distance	Hatch repetitions
Ni CLPs 0°	175 μJ	38.5 J cm^{-2}	v_x, v_y = 6 mm s^{-1}	d_x,d_y = 6 μm	8
Ni CLPs 45°	400 μJ	62.3 J cm^{-2} (on the tilted surface)	v_x = 6 mm s^{-1} v_y = v_z = 3 mm s^{-1}	d_x, d_y, d_z = 6 μm	8

at 140 kV acceleration voltage, 72 μA current, and filtered using a proprietary filter. The distance from the source to the rotating sample axis was set to 9 mm and from rotating sample axis to the detector 20 mm, respectively, resulting in a geometric magnification of 3.2x. A scintillator and 20x optical objective was used to further magnify the image onto a 1024 pixel x 1024 pixel CCD detector, resulting in a voxel size of 425 nm. The estimated reconstructed spatial resolution was 900 nm. 2001 projections with 45 s exposure were taken while the sample was rotated through 360°, resulting in a total scan time of 27 h. Scout-and-Scan Control System Reconstructor software was used to generate the reconstruction. The visualization of the data was done using Dragonfly Pro 3.0 from Object Research Systems. Otsu's thresholding algorithm was used to split the absorption dataset into nickel and epoxy resin-filled cavities. The contact angle measurements were performed on a Krüss Mobile Surface Analyzer with a 1 μL deionized water droplet.

2.3. Electrochemical Characterization. The electrochemical measurements were performed with a Bio-Logic Science Instruments VMP3 potentiostat. A three-electrode-setup with a steel mesh as the counter electrode and an Ag/AgCl (3 M KCl, E = 0.21 V) reference electrode was used, while the Ni plates served as the working electrodes. The working electrodes were placed vertically in the cell. 25 wt.-% KOH (Sigma Aldrich) served as the electrolyte. The cyclic voltammograms (CV) of the laser-structured and tempered Ni plates were recorded between E = -0.50 V and E = 0.52 V versus Ag/AgCl with a scan speed of ν = 20 mV s^{-1}. After the initial recording the linear sweep voltammograms (LSV) were termed "*as prepared*" and after 300 further CV cycles with a scan speed of ν = 10 mV s^{-1}, termed as "*activated*". The long-term stability test was carried out with chronopotentiometry at J = 100 mA cm^{-2} for 48 h. The data were not iR corrected. The OER overpotential was calculated on the basis of (1), with E^0 = 1.229 V. The potential conversion from the recorded $E_{Ag/AgCl}$ to E_{RHE} is given by (2).

$$\eta_{OER} = E_{RHE} - E^0 \quad (1)$$

$$E_{RHE} = E_{Ag/AgCl} + 0.21\,\text{V} + 0.059 \cdot pH \quad (2)$$

The double layer capacitance (C_{dl}) was determined from a CV cascade in a potential window of ΔE = 0.1 V at the open circuit potential (OCP) using the following equation:

$$C_{dl} = \frac{\Delta J}{2\nu} \quad (3)$$

where ΔJ describes the sum of the absolute anodic and cathodic current densities and ν the scan speed. In order to gain further information about the enlargement of the surface area, the roughness factor R_f was determined. For the latter, the double layer capacitance of a structured sample ($C_{dl,structured}$) was divided by the double layer capacitance of the plane reference sample ($C_{dl,plane}$), normalized to 1 cm^2:

$$R_f = \frac{C_{dl,structured}}{C_{dl,plane}} \quad (4)$$

3. Results and Discussion

The laser-structured Ni plates show high periodicity and excellent uniform topography across the whole 1 cm^2 area due to the overlap of parallel laser scans and the repetitive structuring process; see Figure 1. Comparisons between the laser-structured Ni CLPs 0° and Ni CLPs 45° show that the spike's orientation is almost identical to the laser irradiation angle, as the spikes form with an angle of 45° on the Ni plate at a laser irradiation angle of 45°. These observations correspond with previous studies on laser-structured surfaces [38, 45]. The mean distance between the spikes at Ni CLPs 0° is around 15 μm, while the average spike spacing at Ni CLPs 45° is a few micrometers larger. Moreover, the spikes are decorated with redeposited nanosized ablation product. In addition, the hierarchical surface structures exhibit laser-induced ripples. The ripples are not uniformly oriented since the polarization vector of the laser beam was constantly rotated during the processing.

X-ray diffraction (XRD) was carried out to study the crystallinity of the laser-structured and tempered plates (see supplementary information (Available here)). The only phase found in the XRD patterns of the laser-structured plates was elemental nickel. As expected, the pattern of tempered Ni depicted only small signals of a nickel oxide species, which can be assigned to a thin NiO layer. However, EDX analysis of the laser-structured plates exhibited an O K_α signal, indicating the presence of nickel oxide (supplementary information). Since XRD has an information depth of several micrometers [47], XRD measurements contain mostly information about the bulk material. Ni passivates at room temperature in three steps, where the first step is the chemisorption of oxygen at the Ni surface. In a second step, NiO nucleation and lateral growth lead to coalescence and the formation of ≈2 atomic layers of NiO. Over time, NiO growth up to 4 atomic layers [48]. The NiO passivation layer protects the Ni not well enough under high potential applications like OER, and thus, it is necessary to use thicker NiO layers. The

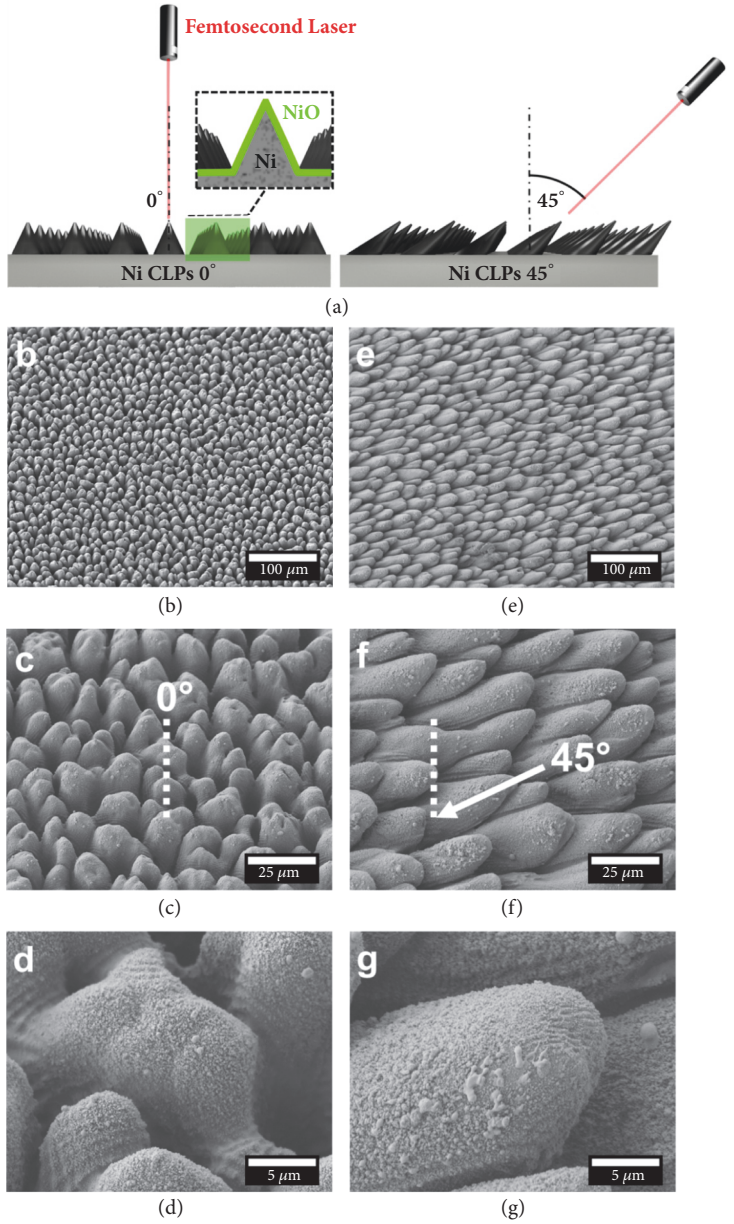

FIGURE 1: (**a**) Schematic illustrations of the preparation process of the laser-structured Ni electrodes in air. The direction of the formed spikes depends on the incident angle of the laser beam; simultaneously oxidation of the Ni surface occurs. (**b**-**g**) SEM images of laser-structured Ni electrodes at different magnifications. The irradiation angle of the laser during the structuring was set to 0° (**b**-**d**) and 45° (**e**-**g**). The SEM images were taken at a sample tilt angle of 25°.

present laser-structured Ni electrodes exhibit thicker oxide layer of 4 to 7 nm (see supplementary information). Usually, the drawback of metal oxide electrocatalysts is their poor electrical conductivity [49].

To determine the surface composition of the *as prepared* tempered and laser-structured Ni electrodes, X-ray photoelectron spectroscopy (XPS) measurements were carried out. In general, the oxidation state of nickel at the surface can be derived from the binding energies and their chemical shifts in the XPS [29]. Besides the laser-structured sample tempered Ni and NiO powder (Alfa Aesar, >99%) was used as reference samples. Figures 2(a) and 2(b) compare the normalized Ni $2p_{3/2}$ spectra as well as the O 1s spectra of the NiO powder, the tempered Ni electrode, and the laser-structured Ni CLPs 0° electrode.

The Ni $2p_{3/2}$ photoelectron transitions of the three samples (around 854 eV) show multiplet splitting and shake-up satellites (at 860 eV), which is typical for nickel oxide species and corresponds well with published data [50, 51]. Unfortunately, the complex main line splitting and the satellite structures at higher binding energies make nickel related XPS challenging to interpret. Similar to the procedure to

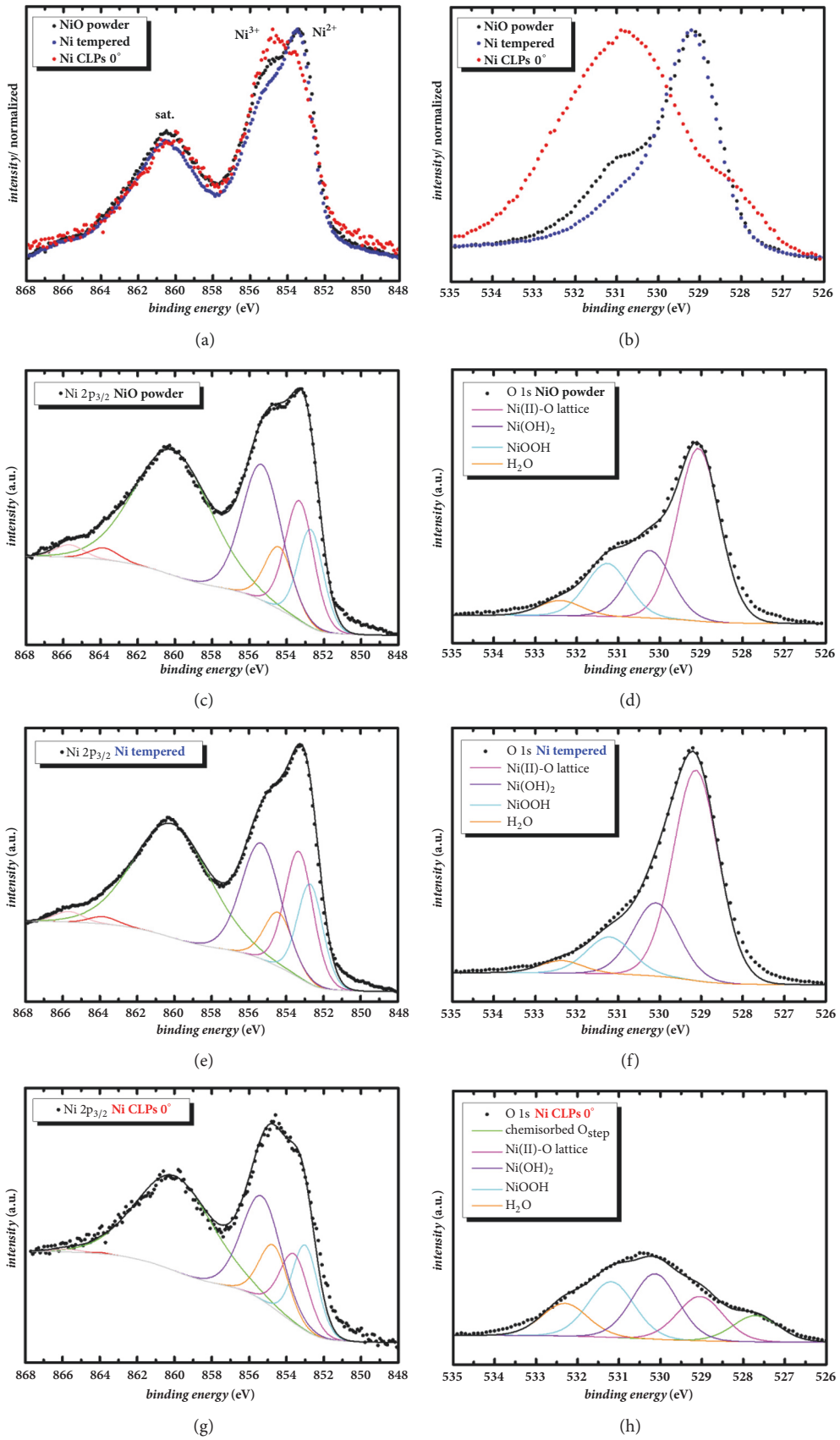

FIGURE 2: Normalized Ni $2p_{3/2}$ X-ray photoelectron spectrum (**a**) and the corresponding O 1s spectrum (**b**) of NiO powder used as reference sample and the tempered as well as laser-structured Ni electrodes. Fitted X-ray photoelectron spectra of NiO powder (**c**-**d**), Ni tempered (**e**-**f**), and Ni CLPs 0° (**g**-**h**). Data were fitted according to Grosvenor et al. [29].

Grosvenor et al. [29] and Biesinger et al. [52] we decomposed the Ni $2p_{3/2}$ and the O 1s signal. After subtraction of a Shirley-type background, four components to fit the Ni $2p_{3/2}$ spectra were used analog to the Ni^{3+} multiplet envelope in Grosvenor et al. [29] (Figures 2(c), 2(e), and 2(g)). The energetic positions of our fit components have been kept constant to allow a better comparison between our three samples. This causes slight deviations between spectra and fit, but do not affect the qualitative comparison. The Ni $2p_{3/2}$ spectrum of the tempered Ni electrode is almost identical to the NiO powder spectrum. As Payne et al. [53] have shown, pure NiO contributes to binding energies between 853 eV and 854 eV. Hence, the main signal at 853.3 eV was attributed to the Ni^{2+} compound in the NiO lattice. The NiO powder spectrum shows a stronger shoulder at higher binding energies as compared to the tempered Ni electrode (see the fit component at 854.4 eV), which is essentially related to the $Ni(OH)_2$ component. $Ni(OH)_2$ forms at the surface of the NiO powder due to exposure to atmosphere. In contrast, the main signal in the spectrum of the laser-structured Ni CLPs 0° electrode is found at 854.9 eV. The ratio of the areas of the four fit components correspond very well with the ratios of the Ni^{3+} multiplet peaks in Grosvernors [29] work. Accordingly, $Ni(OH)_2$ and NiOOH probably became the dominant surface components. As the spectra of both are practically equal, they are difficult to distinguish [54, 55]. Furthermore, the Ni^{3+} compound in NiOOH is chemically identical to NiO lattice defects [55]. Thus, Ni^{3+} related compounds are often interpreted as defects [56] and a clear allocation cannot be made.

The O 1s spectra of the reference NiO powder, of the tempered Ni electrode, and of the Ni CLPs 0° electrode were deconvoluted using four components for the powder as well as for the tempered sample, and five for the Ni CLPs, respectively. The full width at half maximum is kept equal for all the samples and all the components. The allocation to the particular O compound is in agreement with Ratcliff et al. [57]. The surface of the tempered Ni electrode primarily consists of NiO, which confirms the finding from the Ni $2p_{3/2}$ spectrum. The shoulder of the peak was allocated to a hydroxide signal, indicating the presence of $Ni(OH)_2$ and minor contributions of NiOOH as well as adsorbed water. In contrast to the tempered Ni electrode, the Ni CLPs 0° electrode shows dominant signals of $Ni(OH)_2$ and NiOOH species in the O 1s spectrum. Subsequently, the high intensities of the hydroxide species indicate that the transformation of NiO to $Ni(OH)_2$ or NiOOH is favored for the laser-structured surfaces. Again, the XPS signal of NiOOH species can also be interpreted as oxygen defects in the lattice [56]. The fifth component in the O 1s spectrum of the Ni CLPs 0° electrode has unusual low binding energies of about 527.7 eV. Bukhtiyarov et al. [58, 59] described this oxygen species as chemisorbed oxygen at atomic steps (O_{step}). Finally, the X-ray photoelectron spectroscopy (XPS) results in Figures 2(a)–2(h) show a significant difference in the surface composition between the tempered Ni electrode and the laser-structured Ni CLPs 0° electrode. The dominant high-binding-energy components in the Ni $2p_{3/2}$ and the O 1s spectra indicate a higher concentration of $Ni(OH)_2$ and NiOOH at the surface of the laser-structured Ni CLPs 0° electrode. During the laser structuring, the nickel is rapidly heated and thereby transformed into a mixture of liquid droplets and vapor [60]. Due to the fast quenching of the precipitated metal droplets, the solidified metal nanoparticles may show low-coordination sites at steps, cavities or compositional imperfections, which can act as catalytically active sites [61]. Still, the nickel oxide spectra pose a number of obstacles like complex multiplet splitting, satellite appearance and plasmon loss structures, which makes it difficult to assess the nature of the oxidized nickel species in detail [52]. Quantification of mixed nickel chemical states is even more challenging due to the different sample surface morphologies. Hereafter will be discussed how the defect containing structures, created during the laser structuring process, will affect the electrochemical OER behavior.

The laser-structured and the tempered Ni electrodes were evaluated in alkaline electrocatalytic water splitting as the oxygen evolution anode. Figure 3(a) depicts the cyclic voltammograms (CV) recorded between E = -0.50 V and E = 0.52 V versus Ag/AgCl reference electrode. Since there are no electrochemical processes and a non-faradaic current occurs in the potential range of -0.5 V to 0.1 V versus Ag/AgCl, the open circuit potential, which is located in this potential range, is suitable for determining the double layer capacitance [62]. Therefore, CV cascades at varying scan speeds were carried out around the open circuit potential; see supplementary information. The double layer capacitance was calculated by plotting the sum of the absolute anodic and cathodic current densities against the double scan speed. From (1), the double layer capacitance C_{dl} was determined, which was used to calculate the roughness factor R_f according to (2). The resulting data reveal a significant increase of the surface area by a factor of 49 (C_{dl} = 0.97 mF cm^{-2}) for Ni CLPs 0° and 87 for Ni CLPs 45° (C_{dl} = 1.74 mF cm^{-2}), respectively (see Figure 3(b)). Firstly, the surface area enlargement is caused by the formation of micrometer-sized spikes and secondly by a significant amount of a redeposited nanosized ablation product, which covers the spike structure. The present results for Ni CLPs 0° are in good agreement with published data on CLP structures [63, 64].

In order to understand why the surface area of Ni CLPs 45° is roughly two times larger in comparison to Ni CLPs 0°, X-ray microscopy (XRM) analysis was performed on the Ni CLPs 45° sample; see Figures 4(a)–4(c). The non-invasive XRM allows recording high quality 3D images with submicrometer resolution based on material density. In the SEM images shown above (Figure 1), it can be clearly seen that the flanks of the tilted spikes (Ni CLPs 45°) are larger than the flanks of the Ni CLPs 0° spikes. However, with SEM the backside of the tilted spikes cannot be studied. Thus, it is non-trivial to assess the contribution of the backsides of the tilted spikes to the double layer capacitance. As highlighted in Figure 4(c), however, there are deep cavities between the tilted spikes, which allow the electrolyte to reach the backside of the tilted spikes. Thus, the backsides of the tilted spikes seem to contribute significantly to the double layer

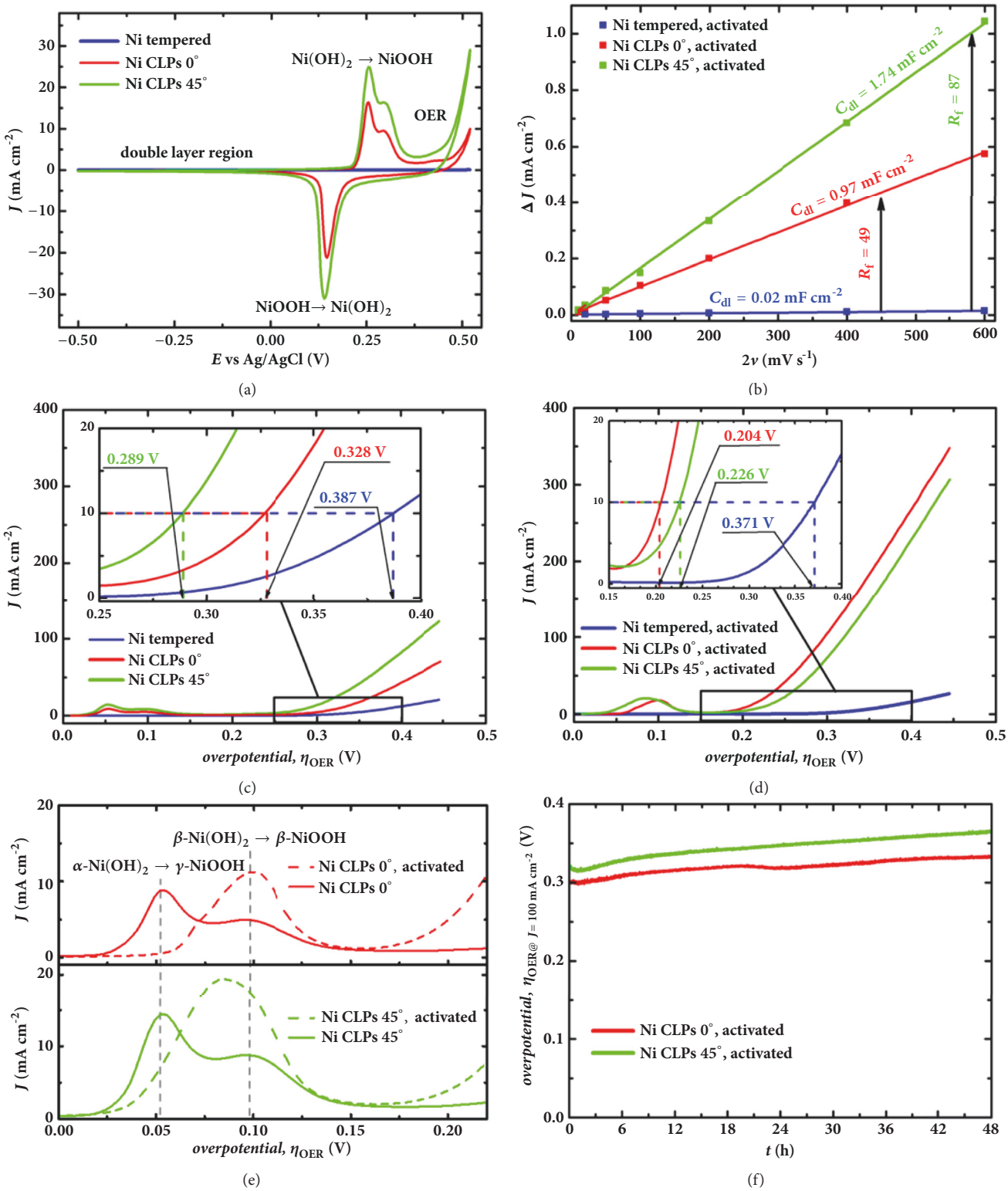

FIGURE 3: Cyclic voltammograms (CV) of *as prepared* laser-structured and tempered Ni plates (**a**) with a scan speed of $\nu = 20$ mV s^{-1}. All electrochemical measurements were performed in 25 wt.-% KOH solution at room temperature. The sum of the absolute anodic and cathodic current densities versus the scan speed ν (**b**). The slope of the resulting fit curves corresponds to the double layer capacitances of tempered and laser-structured Ni electrodes. The corresponding CV cascades can be found in the supplementary information. CVs were carried out at nonfaradaic regions in a potential window of $\Delta E = 0.1$ V around the open circuit potential. Linear sweep voltammograms *as prepared* (**c**) and *activated* (**d**) recorded with a scan speed of $\nu = 10$ mV s^{-1}. Inset: magnifications of the area at $J = 10$ mA cm^{-2} with markings highlighting the corresponding overpotentials at $J = 10$ mA cm^{-2}. Magnified linear sweep voltammograms in the potential region of the $Ni(OH)_2$ to NiOOH oxidation (**e**). Chronopotentiometric curves for long-term stability of the water electrolysis electrodes at a current density of $J = 100$ mA cm^{-2} (**f**).

Table 2: Overview of key indications: double layer capacitance C_{dl} and the corresponding roughness factor R_f as well as the oxygen evolution overpotential η_{OER} @ 10 mA cm^{-2} of the tempered Ni electrode and the laser-structured samples Ni CLPs 0° and Ni CLPs 45° *as prepared* and *activated*.

Sample name	C_{dl}	R_f	η_{OER}@ 10 mA cm^{-2} *as prepared*	η_{OER}@ 10 mA cm^{-2} *activated*
Ni tempered	0.02 mF cm^{-2}	1	0.387 V	0.371 V
Ni CLPs 0°	0.97 mF cm^{-2}	49	0.328 V	0.204 V
Ni CLPs 45°	1.74 mF cm^{-2}	87	0.289 V	0.226 V

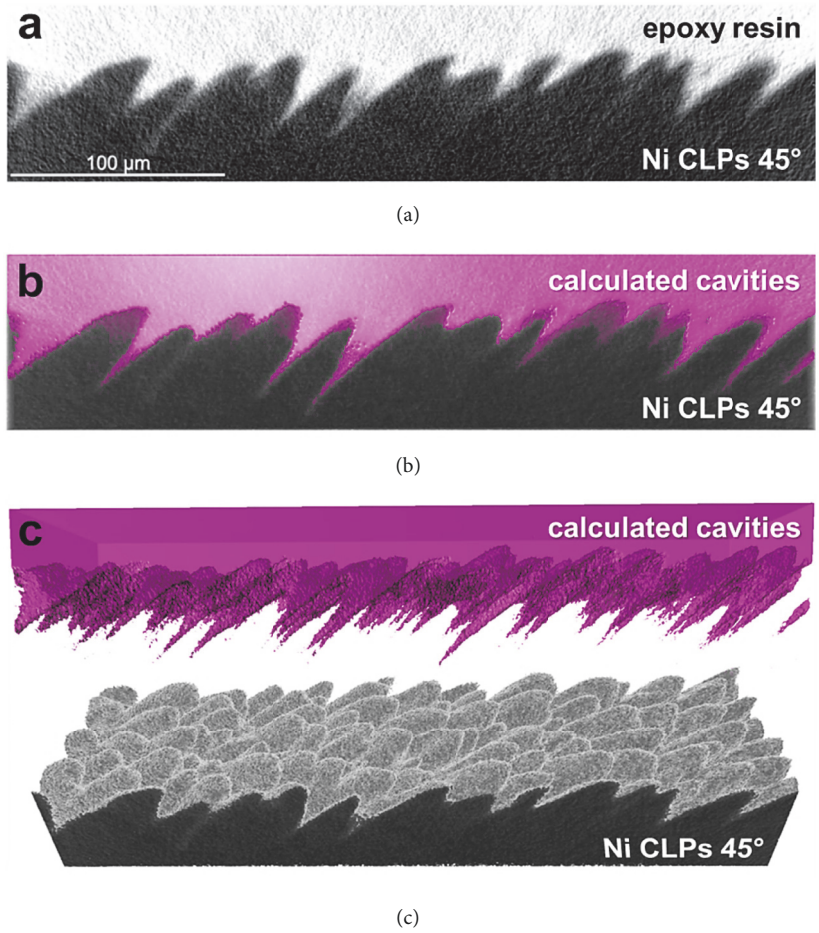

Figure 4: X-ray microscopy (XRM) data showing (**a**) absorption-contrast image of Ni CLPs 45° and representative density information. Reconstruction of the cavities within the Ni CLPs 45° structure based on absorption contrast of infiltrated epoxy resin in 2D (**b**) and 3D visualization (**c**).

capacitance and provide more surface area than in the case of the Ni CLPs 0° spikes.

According to Lyons et al. [14], the redox couple between E = 0.10 V and E = 0.40 V versus Ag/AgCl in Figure 3(a) corresponds to the oxidation of $Ni(OH)_2$ into NiOOH, which is a highly active intermediate within the OER [65]. This kind of layer-structure oxide usually exhibits good electric conductivity and has been used in alkaline batteries since the 1970s [49]. LSV of the *as prepared* electrodes were conducted to investigate their electrocatalytic behavior as OER anodes; see Figure 3(c). At the NiO alkaline electrolyte interface α-$Ni(OH)_2$ (3 $Ni(OH)_2$• 2 H_2O) is instantaneously formed [66]. α-$Ni(OH)_2$ is the hydrated species of β-$Ni(OH)_2$ and can be electrochemically oxidized to γ-NiOOH. In alkaline media α-$Ni(OH)_2$ is slowly transformed irreversibly into β-$Ni(OH)_2$ via an aging process [9]. Through electrochemical oxidization, β-$Ni(OH)_2$ is converted into β-NiOOH, which is commonly called "the right type of oxide" due to its excellent catalytic OER activity [14]. In the LSV, the conversion of β-$Ni(OH)_2$ to β-NiOOH appears shifted approximately 40 mV towards higher potentials in comparison with the conversion of α-$Ni(OH)_2$ to γ-NiOOH [66]. In the present activation process, α-$Ni(OH)_2$ is transformed into β-$Ni(OH)_2$ and therefore directs the oxidation to the preferred highly active β-NiOOH species. The corresponding LSV curves are shown in Figure 3(d). Furthermore, Table 2 compares the

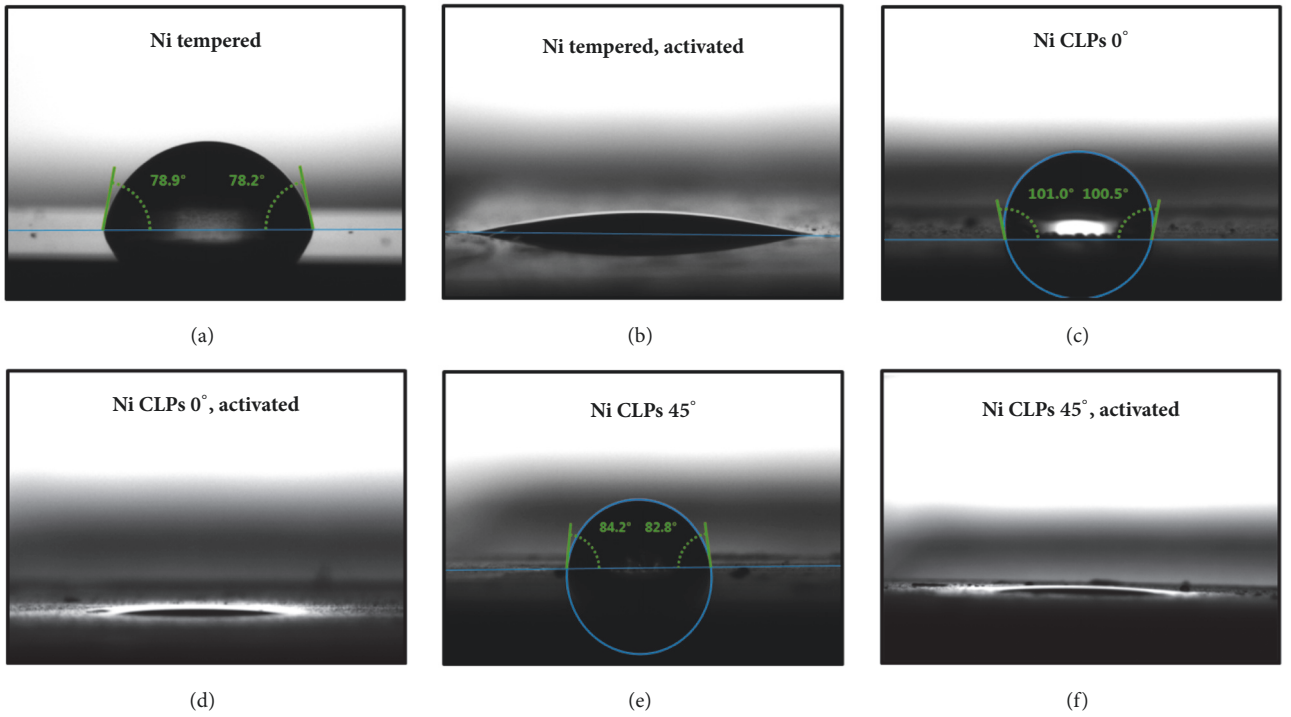

Figure 5: Contact angle measurements of the tempered Ni plate as prepared (a) and activated (b), Ni CLPs 0° as prepared (c) and activated (d), and Ni CLPs 45° as prepared (e) and activated (f). The measurements were carried out with a deionized water droplet (V = 1 μL). The activated electrodes show superhydrophilic behavior; therefore determination of the contact angle was not possible.

overpotentials at a current density of 10 mA cm^{-2} of the *as prepared* and *activated* electrodes. The *as prepared* laser-structured electrodes exhibit a noticeable improvement compared to the tempered one, where the *as prepared* Ni CLPs 45° (0.289 V) is slightly more active than the *as prepared* Ni CLPs 0° (0.328 V). Surprisingly, after the activation process the *activated* Ni CLPs 0° has the lowest overpotential (0.204 V) of all three samples. The Ni CLPs 0° electrode undergoes a complete conversion of α-Ni(OH)$_2$ to β-Ni(OH)$_2$ via the activation process and therefore a total transformation to the active β-NiOOH could be observed. In contrast, the Ni CLPs 45° electrode shows incomplete conversion of α-Ni(OH)$_2$ to β-Ni(OH)$_2$; see Figure 3(e).

Additionally, the maximum current density of Ni CLPs 0° is 10% higher than Ni CLPs 45°. In contrast, the expected performance of the Ni CLPs 45° electrode based on the roughness factor was significantly higher compared to the Ni CLPs 0° electrode. Especially at high current densities heavy gas evolution occurs and consequently bubble detachment becomes crucial.

To improve the bubble detachment during a gas evolution reaction, the electrode surface should be enhanced with respect to their wettability, resulting in decreased bubble-electrode attraction. Thus, the electrolyte can replace the bubbles on the electrocatalytic sites more easily. The *as prepared* tempered Ni plate as well as the laser-structured Ni CLPs 0° plate and Ni CLPs 45° plate revealed high contact angles of approximately 78°, 101° and 83°. As expected, the activation process clearly improves the wettability due to the formation of Ni(OH)$_2$ and NiOOH. Superhydrophilicity was observed on all types of electrodes; see Figure 5. That is probably the reason why our structured Ni CLPs electrodes outperform differently laser-structured electrodes studied by Ou et al. [67] in terms of their overall OER performance.

Nevertheless, the direct investigation of gas evolution on electrode surfaces remains challenging especially for coarse, not plane, electrodes like our spike structures. Zeradjanin et al. [68] was able to prove the existence of a link between surface morphology and the overall catalytic performance. Thus, the microstructure of the electrode surface has to be considered for the improvement of the efficiency of gas evolution electrodes. Hence, the electrochemical results indicate that the vertical Ni CLPs 0° electrode support more rapid gas bubble detachment compared to the Ni CLPs 45° electrode. But it has to be mentioned that we were not able to determine the actual gas bubble detachment frequencies of the laser-structured samples.

Electrochemical stability and durability tests (Figure 3(f)) were carried out under demanding conditions at 100 mA cm^{-2} for 48 h to assess the suitability as a long-term working OER electrode. Chronopotentiometry is found to be an appropriate and fast method to evaluate the electrochemical stability of such electrodes [69]. In the process, both types of laser-structured Ni electrodes exhibited only a slight increase of the overpotential during the test period, indicating excellent electrochemical stability

at high current densities. Thus, there is a stable adhesion of the catalytic active nanodecorations on the conducting CLP structures, which enable long-term process stability for OER applications. Furthermore, all electrodes show a similar Tafel slope of approximately 60 mV dec^{-1}, indicating that a chemical step is rate-determining for all different electrode types [11, 70, 71]. The corresponding Tafel plots can be found in the supplementary information. However, many different electrochemical processes may influence the slope of gas evolution electrodes especially at high current densities like mass transfer problems (varying depletion zone) [72]: bubble adhesion, coalescence, and detachment causing limiting current behavior [73].

4. Conclusion

A femtosecond laser was used as a novel tool for the generation of ordered nano- and microstructures on bulk Ni substrates. Two types of Ni/NiO spiky microstructures were created through variation of the incident angle of the laser beam and tested as electrodes for electrochemical water splitting. Currently, the oxygen evolution reaction (OER) is a key limiting factor for water splitting. Both investigated laser-structured Ni electrodes exhibited an increase in OER performance by more than one order of magnitude compared to a plane tempered Ni reference sample. Furthermore, the OER overpotential was decreased by over 100 mV compared to the reference sample. Based on X-ray photoemission spectroscopy data, this could be attributed to the formation of catalytic active defect sites at the surface of the laser-structured electrodes. Due to the high cooling rates within the laser structuring process, the nanosized decoration on the spikes shows a higher emergence of steps, cavities, low-coordination sites, and compositional imperfections, that all can act as catalytic active sites. This favors the formation of highly active NiOOH species on the laser-structured electrodes. In addition, femtosecond laser structuring combines excellent versatility and compatibility and is easy to adapt to other metal or semiconductor materials.

Data Availability

The XRD data used to support the findings of this study are included within the supplementary information file(s). The EDXS data used to support the findings of this study are included within the supplementary information file(s). The XRD and EDXS raw data used to support the findings of this study are available from the corresponding author upon request. The contact angle data used to support the findings of this study are included within the supplementary information file(s). The CV and LSV data used to support the findings of this study are available from the corresponding author upon request.

Conflicts of Interest

The authors declare that they have no conflicts of interest.

Acknowledgments

This study was conducted within the framework of the ElektroBak graduate program organized by Uwe Schröder (TU Braunschweig). Furthermore, the authors thank the Laser Zentrum Hannover e.V. for the laser structuring, the technical expertise, and general support, as well as Wanja Dziony (TU Clausthal) for the XPS measurements. The X-ray microscope used has been funded by the German Research Foundation under Contract MA 1175/67-1 as part of its major instrumentation initiative. In addition, they thank Frank Steinbach for the preparation of the X-ray microscopy sample.

Supplementary Materials

Supplementary material contains X-ray diffraction patterns of the laser-structured Ni electrodes and the tempered comparative sample as well as an energy-dispersive X-ray spectrum and an elementary depth profile of a laser-structured Ni electrode. Furthermore, cyclic voltammogram cascades of all samples carried out around the open circuit potential are given. Finally, Tafel plots of the laser-structured Ni electrodes and the tempered comparative sample are included. *(Supplementary Materials)*

References

[1] W. C. Sheng, H. A. Gasteiger, and Y. J. Shao-Horn, "Hydrogen oxidation and evolution reaction kinetics on platinum: acid vs alkaline electrolytes," *Journal of The Electrochemical Society*, vol. 157, no. 11, pp. B1529–B1536, 2010.

[2] I. E. L. Stephens and I. Chorkendorff, "Minimizing the use of platinum in hydrogen-evolving electrodes," *Angewandte Chemie International Edition*, vol. 50, no. 7, pp. 1476-1477, 2011.

[3] D. M. Santos, C. A. Sequeira, and J. L. Figueiredo, "Hydrogen production by alkaline water electrolysis," *Química Nova*, vol. 36, no. 8, pp. 1176–1193, 2013.

[4] M. T. M. Koper, "Thermodynamic theory of multi-electron transfer reactions: Implications for electrocatalysis," *Journal of Electroanalytical Chemistry*, vol. 660, no. 2, pp. 254–260, 2011.

[5] J. Rossmeisl, A. Logadottir, and J. K. Nørskov, "Electrolysis of water on (oxidized) metal surfaces," *Chemical Physics*, vol. 319, no. 1-3, pp. 178–184, 2005.

[6] A. Michas, F. Andolfatto, M. Lyons, and R. Durand, "Gas Evolution Reactions at Conductive Metallic Oxide Electrodes for Solid Polymer Electrolyte Water Electrolysis," *Key Engineering Materials*, vol. 72-74, pp. 535–550, 1992.

[7] E. Rasten, G. Hagen, and R. Tunold, "Electrocatalysis in water electrolysis with solid polymer electrolyte," *Electrochimica Acta*, vol. 48, no. 25-26, pp. 3945–3952, 2003.

[8] M. E. G. Lyons and S. Floquet, "Mechanism of oxygen reactions at porous oxide electrodes. Part 2—Oxygen evolution at RuO_2, IrO_2 and $Ir_xRu_{1-x}O_2$ electrodes in aqueous acid and alkaline solution," *Physical Chemistry Chemical Physics*, vol. 13, no. 12, pp. 5314–5335, 2011.

[9] I. J. Godwin and M. E. G. Lyons, "Enhanced oxygen evolution at hydrous nickel oxide electrodes via electrochemical ageing in alkaline solution," *Electrochemistry Communications*, vol. 32, pp. 39–42, 2013.

[10] J. Wang, W. Cui, Q. Liu, Z. Xing, A. M. Asiri, and X. Sun, "Recent Progress in Cobalt-Based Heterogeneous Catalysts for Electrochemical Water Splitting," *Advanced Materials*, vol. 28, no. 2, pp. 215–230, 2016.

[11] M. E. G. Lyons and M. P. Brandon, "A comparative study of the oxygen evolution reaction on oxidised nickel, cobalt and iron electrodes in base," *Journal of Electroanalytical Chemistry*, vol. 641, no. 1-2, pp. 119–130, 2010.

[12] F. Jiao and H. Frei, "Nanostructured cobalt oxide clusters in mesoporous silica as efficient oxygen-evolving catalysts," *Angewandte Chemie International Edition*, vol. 48, no. 10, pp. 1841–1844, 2009.

[13] I. Nikolov, R. Darkaoui, E. Zhecheva, R. Stoyanova, N. Dimitrov, and T. Vitanov, "Electrocatalytic activity of spinel related cobalties $M_xCo_{3-x}O_4$ (M = Li, Ni, Cu) in the oxygen evolution reaction," *Journal of Electroanalytical Chemistry*, vol. 429, no. 1-2, pp. 157–168, 1997.

[14] M. E. G. Lyons and M. P. Brandon, "The oxygen evolution reaction on passive oxide covered transition metal electrodes in aqueous alkaline solution. Part 1-Nickel," *International Journal of Electrochemical Science*, vol. 3, no. 12, pp. 1386–1424, 2008.

[15] L. Sigrist, O. Dossenbach, and N. Ibl, "Mass transport in electrolytic cells with gas sparging," *International Journal of Heat and Mass Transfer*, vol. 22, no. 10, pp. 1393–1399, 1979.

[16] K. Zeng and D. Zhang, "Recent progress in alkaline water electrolysis for hydrogen production and applications," *Progress in Energy and Combustion Science*, vol. 36, no. 3, pp. 307–326, 2010.

[17] T. Burdyny, P. J. Graham, Y. Pang et al., "Nanomorphology-Enhanced Gas-Evolution Intensifies CO_2 Reduction Electrochemistry," *ACS Sustainable Chemistry & Engineering*, vol. 5, no. 5, pp. 4031–4040, 2017.

[18] K. Wang, P. Pei, Z. Ma et al., "Growth of oxygen bubbles during recharge process in zinc-air battery," *Journal of Power Sources*, vol. 296, pp. 40–45, 2015.

[19] M. Wang, Z. Wang, and Z. Guo, "Water electrolysis enhanced by super gravity field for hydrogen production," *International Journal of Hydrogen Energy*, vol. 35, no. 8, pp. 3198–3205, 2010.

[20] W. Kim, K. Park, J. Oh, J. Choi, and H.-Y. Kim, "Visualization and minimization of disruptive bubble behavior in ultrasonic field," *Ultrasonics*, vol. 50, no. 8, pp. 798–802, 2010.

[21] S.-D. Li, C.-C. Wang, and C.-Y. Chen, "Water electrolysis in the presence of an ultrasonic field," *Electrochimica Acta*, vol. 54, no. 15, pp. 3877–3883, 2009.

[22] S. Marini, P. Salvi, P. Nelli et al., "Advanced alkaline water electrolysis," *Electrochimica Acta*, vol. 82, pp. 384–391, 2012.

[23] A. R. Zeradjanin, A. A. Topalov, Q. Van Overmeere et al., "Rational design of the electrode morphology for oxygen evolution-enhancing the performance for catalytic water oxidation," *RSC Advances*, vol. 4, no. 19, pp. 9579–9587, 2014.

[24] D. Kiuchi, H. Matsushima, Y. Fukunaka, and K. Kuribayashi, "Ohmic resistance measurement of bubble froth layer in water electrolysis under microgravity," *Journal of The Electrochemical Society*, vol. 153, no. 8, pp. E138–E143, 2006.

[25] H. Matsushima, Y. Fukunaka, and K. Kuribayashi, "Water electrolysis under microgravity. Part II. Description of gas bubble evolution phenomena," *Electrochimica Acta*, vol. 51, no. 20, pp. 4190–4198, 2006.

[26] C. Tang, N. Cheng, Z. Pu, W. Xing, and X. Sun, "NiSe Nanowire Film Supported on Nickel Foam: An Efficient and Stable 3D Bifunctional Electrode for Full Water Splitting," *Angewandte Chemie International Edition*, vol. 54, no. 32, pp. 9351–9355, 2015.

[27] T. Y. Ma, S. Dai, M. Jaroniec, and S. Z. Qiao, "Metal-organic framework derived hybrid Co_3O_4-carbon porous nanowire arrays as reversible oxygen evolution electrodes," *Journal of the American Chemical Society*, vol. 136, no. 39, pp. 13925–13931, 2014.

[28] Y. Fukunaka, M. Motoyama, Y. Konishi, and R. Ishii, "Producing shape-controlled metal nanowires and nanotubes by an electrochemical method," *Electrochemical and Solid-State Letters*, vol. 9, no. 3, pp. C62–C64, 2006.

[29] A. P. Grosvenor, M. C. Biesinger, R. S. C. Smart, and N. S. McIntyre, "New interpretations of XPS spectra of nickel metal and oxides," *Surface Science*, vol. 600, no. 9, pp. 1771–1779, 2006.

[30] P. Russbueldt, T. Mans, J. Weitenberg, H. D. Hoffmann, and R. Poprawe, "Compact diode-pumped 1.1 kW Yb:YAG Innoslab femtosecond amplifier," *Optics Expresss*, vol. 35, no. 24, pp. 4169–4171, 2010.

[31] T. Mans, J. Dolkemeyer, and C. Schnitzler, "High Power Femtosecond Lasers," *Laser Technik Journal*, vol. 11, no. 3, pp. 40–43, 2014.

[32] B. K. Nayak and M. C. Gupta, "Self-organized micro/nano structures in metal surfaces by ultrafast laser irradiation," *Optics and Lasers in Engineering*, vol. 48, no. 10, pp. 940–949, 2010.

[33] S. Bruening, G. Hennig, S. Eifel, and A. Gillner, "Ultrafast Scan Techniques for 3D-μm Structuring of Metal Surfaces with high repetitive ps-laser pulses," *Physics Procedia*, vol. 12, pp. 105–115, 2011.

[34] M. Tsukamoto, T. Kayahara, H. Nakano et al., "Microstructures formation on titanium plate by femtosecond laser ablation," *Journal of Physics: Conference Series*, vol. 59, pp. 666–669, 2007.

[35] K. M. Tanvir Ahmmed, C. Grambow, and A.-M. Kietzig, "Fabrication of micro/nano structures on metals by femtosecond laser micromachining," *Micromachines*, vol. 5, no. 4, pp. 1219–1253, 2014.

[36] E. Fadeeva, S. Schlie, J. Koch, B. N. Chichkov, A. Y. Yorobyev, and C. Guo, "Femtosecond Laser-Induced Surface Structures on Platinum and Their Effects on Surface Wettability and Fibroblast Cell Proliferation," in *Contact Angle, Wettability and Adhesion*, K. L. Mittal, Ed., vol. 6, pp. 163–171, CRC Press, Leiden, Netherlands, 2009.

[37] A. Gabler, C. I. Müller, T. Rauscher et al., "Ultrashort-pulse laser structured titanium surfaces with sputter-coated platinum catalyst as hydrogen evolution electrodes for alkaline water electrolysis," *International Journal of Hydrogen Energy*, vol. 43, no. 15, pp. 7216–7226, 2018.

[38] T. Yong Hwang and C. Guo, "Polarization and angular effects of femtosecond laser-induced conical microstructures on Ni," *Journal of Applied Physics*, vol. 111, no. 8, p. 083518, 2012.

[39] T. Jiang, J. Koch, C. Unger et al., "Ultrashort picosecond laser processing of micro-molds for fabricating plastic parts with superhydrophobic surfaces," *Applied Physics A: Materials Science & Processing*, vol. 108, no. 4, pp. 863–869, 2012.

[40] D. Kam, J. Kim, L. Song, and J. Mazumder, "Formation mechanism of micro-spikes on AISI 4340 steel with femtosecond laser pulses at near-threshold fluence," *Journal of Micromechanics and Microengineering*, vol. 25, no. 4, p. 045007, 2015.

[41] B. K. Nayak, V. V. Iyengar, and M. C. Gupta, "Efficient light trapping in silicon solar cells by ultrafast-laser-induced self-assembled micro/nano structures," *Progress in Photovoltaics*, vol. 19, no. 6, pp. 631–639, 2011.

[42] J. Bonse, S. Baudach, J. Krüger, W. Kautek, and M. Lenzner, "Femtosecond laser ablation of silicon-modification thresholds and morphology," *Applied Physics A: Materials Science & Processing*, vol. 74, no. 1, pp. 19–25, 2002.

[43] B. N. Chichkov, C. Momma, S. Nolte, F. Alvensleben, and A. Tünnermann, "Femtosecond, picosecond and nanosecond laser ablation of solids," *Applied Physics A Materials Science & Processing*, vol. 63, no. 2, pp. 109–115, 1996.

[44] A. Semerok, B. Sallé, J.-F. Wagner, and G. Petite, "Femtosecond, picosecond, and nanosecond laser microablation: Laser plasma and crater investigation," *Laser and Particle Beams*, vol. 20, no. 1, pp. 67–72, 2002.

[45] T. Y. Hwang and C. Guo, "Angular effects of nanostructure-covered femtosecond laser induced periodic surface structures on metals," *Journal of Applied Physics*, vol. 108, no. 7, p. 073523, 2010.

[46] C. Kruse, I. Somanas, T. Anderson et al., "Self-propelled droplets on heated surfaces with angled self-assembled micro/nanostructures," *Microfluidics and Nanofluidics*, vol. 18, no. 5-6, pp. 1417–1424, 2015.

[47] M. Grasserbauer, "Micro and surface analysis for environmental studies," *Microchimica Acta*, vol. 81, no. 5-6, pp. 415–448, 1983.

[48] S. L. Medway, C. A. Lucas, A. Kowal, R. J. Nichols, and D. Johnson, "In situ studies of the oxidation of nickel electrodes in alkaline solution," *Journal of Electroanalytical Chemistry*, vol. 587, no. 1, pp. 172–181, 2006.

[49] N.-T. Suen, S.-F. Hung, Q. Quan, N. Zhang, Y.-J. Xu, and H. M. Chen, "Electrocatalysis for the oxygen evolution reaction: Recent development and future perspectives," *Chemical Society Reviews*, vol. 46, no. 2, pp. 337–365, 2017.

[50] K. S. Kim, "X-ray and UV photoemission studies of valence electronic structure of NiO," *Chemical Physics Letters*, vol. 26, no. 2, pp. 234–239, 1974.

[51] A. M. Venezia, R. Bertoncello, and G. Deganello, "X-ray photoelectron spectroscopy investigation of pumice-supported nickel catalysts," *Surface and Interface Analysis*, vol. 23, no. 4, pp. 239–247, 1995.

[52] M. C. Biesinger, B. P. Payne, A. P. Grosvenor, L. W. M. Lau, A. R. Gerson, and R. S. C. Smart, "Resolving surface chemical states in XPS analysis of first row transition metals, oxides and hydroxides: Cr, Mn, Fe, Co and Ni," *Applied Surface Science*, vol. 257, no. 7, pp. 2717–2730, 2011.

[53] B. P. Payne, P. G. Keech, and N. S. McIntyre, "X-ray photoelectron study of oxides formed on Ni metal and Ni-Cr alloy surfaces under electrochemical control at 25 ∘C and 150 ∘C," *Surface and Interface Analysis*, vol. 49, no. 13, pp. 1316–1324, 2017.

[54] K. K. Lian, "Investigation of a "Two-State" Tafel Phenomenon for the Oxygen Evolution Reaction on an Amorphous Ni-Co Alloy," *Journal of The Electrochemical Society*, vol. 142, no. 11, p. 3704, 1995.

[55] M. C. Biesinger, B. P. Payne, L. W. M. Lau, A. Gerson, and R. S. C. Smart, "X-ray photoelectron spectroscopic chemical state quantification of mixed nickel metal, oxide and hydroxide systems," *Surface and Interface Analysis*, vol. 41, no. 4, pp. 324–332, 2009.

[56] M. W. Roberts and R. S. C. Smart, "The defect structure of nickel oxide surfaces as revealed by photoelectron spectroscopy," *Journal of the Chemical Society, Faraday Transactions 1: Physical Chemistry in Condensed Phases*, vol. 80, no. 11, pp. 2957–2968, 1984.

[57] E. L. Ratcliff, J. Meyer, K. X. Steirer et al., "Evidence for near-surface NiOOH species in solution-processed NiO_x selective interlayer materials: Impact on energetics and the performance of polymer bulk heterojunction photovoltaics," *Chemistry of Materials*, vol. 23, no. 22, pp. 4988–5000, 2011.

[58] V. Bukhtiyarov, A. Boronin, and V. Savchenko, "Two oxygen states and the role of carbon in partial oxidation of ethylene over silver," *Surface Science*, vol. 232, no. 1-2, pp. L205–L209, 1990.

[59] V. I. Bukhtiyarov, M. Hävecker, V. V. Kaichev, A. Knop-Gericke, R. W. Mayer, and R. Schlögl, "Atomic oxygen species on silver: Photoelectron spectroscopy and x-ray absorption studies," *Physical Review B: Condensed Matter and Materials Physics*, vol. 67, no. 23, 2003.

[60] C. Wu and L. V. Zhigilei, "Microscopic Mechanisms of Laser Spallation and Ablation of Metal Targets from Large-Scale Molecular Dynamics Simulations," *Applied Physics A: Materials Science and Processing*, vol. 114, pp. 11–32, 2014.

[61] K. Lange, M. Schulz-Ruhtenberg, and J. Caro, "Platinum Electrodes for Oxygen Reduction Catalysis Designed by Ultrashort Pulse Laser Structuring," *ChemElectroChem*, vol. 4, no. 3, pp. 570–576, 2017.

[62] R. K. Shervedani and A. R. Madram, "Kinetics of hydrogen evolution reaction on nanocrystalline electrodeposited Ni62Fe35C3 cathode in alkaline solution by electrochemical impedance spectroscopy," *Electrochimica Acta*, vol. 53, no. 2, pp. 426–433, 2007.

[63] A. Gabler, C. I. Müller, T. Rauscher et al., "Ultrashort pulse laser-structured nickel surfaces as hydrogen evolution electrodes for alkaline water electrolysis," *International Journal of Hydrogen Energy*, vol. 42, no. 16, pp. 10826–10833, 2017.

[64] T. Rauscher, C. I. Müller, A. Gabler et al., "Femtosecond-laser structuring of Ni electrodes for highly active hydrogen evolution," *Electrochimica Acta*, vol. 247, pp. 1130–1139, 2017.

[65] J. S. Buchanan and L. M. Peter, "Photocurrent spectroscopy of the lead electrode in sulphuric acid," *Electrochimica Acta*, vol. 33, no. 1, pp. 127–136, 1988.

[66] H. Bode, K. Dehmelt, and J. Witte, "Zur Kenntnis der Nickelhydroxidelektrode-I. Über das Nickel (II)-hydroxidhydrat*," *Electrochimica Acta*, vol. 11, no. 8, pp. 1079–1087, 1966.

[67] G. Ou, P. Fan, H. Zhang et al., "Large-Scale Hierarchical Oxide Nanostructures for High-Performance Electrocatalytic Water Splitting," *Nano Energy*, vol. 35, pp. 207–214, 2017.

[68] A. R. Zeradjanin, E. Ventosa, A. S. Bondarenko, and W. Schuhmann, "Evaluation of the catalytic performance of gas-evolving electrodes using local electrochemical noise measurements," *ChemSusChem*, vol. 5, no. 10, pp. 1905–1911, 2012.

[69] J. Bobacka, "Potential stability of all-solid-state ion-selective electrodes using conducting polymers as ion-to-electron transducers," *Analytical Chemistry*, vol. 71, no. 21, pp. 4932–4937, 1999.

[70] B. E. Conway and P. L. Bourgault, "Significance of e.m.f. decay measurements. Applications to the nickel oxide electrode," *Transactions of the Faraday Society*, vol. 58, pp. 593–607, 1962.

[71] B. E. Conway and M. Salomon, "Electrochemical reaction orders: Applications to the hydrogen- and oxygen-evolution reactions," *Electrochimica Acta*, vol. 9, no. 12, pp. 1599–1615, 1964.

[72] M. L. Perry, "Mass Transport in Gas-Diffusion Electrodes: A Diagnostic Tool for Fuel-Cell Cathodes," *Journal of The Electrochemical Society*, vol. 145, no. 1, p. 5, 1998.

[73] J. Eigeldinger and H. Vogt, "The bubble coverage of gas-evolving electrodes in a flowing electrolyte," *Electrochimica Acta*, vol. 45, no. 27, pp. 4449–4456, 2000.